Applied Catalysis B: Environment and Energy 367 (2025) 125105

Contents lists available at ScienceDirect

Applied Catalysis B: Environment and Energy

journal homepage: www.elsevier.com/locate/apcatb

Lattice-mismatched MOF-on-MOF nanosheets with rich oxygen vacancies show fast oxygen evolution kinetics for large-current water splitting

Haoran Yin [a], Menghan Huang [a], Lixia Wang [a], Sheraz Muhammad [a], Tayirjan Taylor Isimjan [d], Jingya Guo [a,*], Dandan Cai [b,*], Bao Wang [c], Xiulin Yang [a,*]

[a] Guangxi Key Laboratory of Low Carbon Energy Materials, School of Chemistry and Pharmaceutical Sciences, Guangxi Normal University, Guilin 541004, China
[b] National Engineering Research Center for Carbohydrate Synthesis, Key Laboratory of Fluorine and Silicon for Energy Materials and Chemistry of Ministry of Education, School of Chemical Engineering, Jiangxi Normal University, Nanchang 330022, China
[c] State Key Laboratory of Biochemical Engineering, Institute of Process Engineering, Chinese Academy of Sciences, Beijing 100190, China
[d] Saudi Arabia Basic Industries Corporation (SABIC) at King Abdullah University of Science and Technology (KAUST), Thuwal 23955-6900, Saudi Arabia

ARTICLE INFO

Keywords:
Heterojunction
Oxygen vacancies
MOF on MOF
Synergistic effect
Water splitting

ABSTRACT

Constructing defective heterojunctions is crucial for enhancing the intrinsic activity of metal-organic framework (MOF)-based electrocatalysts for efficient alkaline water splitting, yet it remains a significant challenge. Here, we present a novel oxygen-vacancy-rich MOF-on-MOF heterojunction nanosheet catalyst (Ni NDC@Fe BDC/CP) fabricated on carbon fiber paper through lattice mismatch. Experimental and theoretical analyses reveal that this catalyst, with an ultra-thin nanosheet morphology (~ 4.3 nm), abundant oxygen defects, and a tightly coupled heterojunction interface, facilitate interfacial charge transport. It optimizes the d-band center, enhances oxygen-containing intermediate adsorption, and promotes the formation of highly active Ni(Fe)OOH species, significantly boosting OER performance. In comparison to individual Ni NDC/CP and Fe BDC/CP, the obtained Ni NDC@Fe BDC/CP exhibits competitive OER performance, delivering an overpotential of 192/239 mV at a current density of 10/100 mA cm^{-2} and a small Tafel slope of 38.8 mV dec^{-1}. When coupled with Pt/C/CP in an overall water splitting device, the Ni NDC@Fe BDC/$CP^{(+)}$||Pt/C/$CP^{(-)}$ achieves a cell voltage as low as 1.43 and 1.54 V at 10 and 100 mA cm^{-2}, respectively, surpassing benchmark catalysts RuO_2 and Pt/C.

1. Introduction

Electrochemical water splitting emerges as a viable solution for hydrogen production in the urgent pursuit of meeting carbon neutrality targets [1]. This process encompasses two essential half-reactions: oxygen evolution reaction (OER) and hydrogen evolution reaction (HER). Generally, OER is a complex electron transfer process involving O-H bond breaking and O═O bond formation, poses a significant challenge to water splitting efficiency (OER, $4OH^- \rightarrow 2H_2O + O_2 + 4e^-$) [2,3]. Currently, Ir/Ru-based catalysts are prevalent for accelerating OER, yet their high costs and limited productivity necessitate exploration into alternative cost-effective and efficient electrocatalysts [4]. Despite the discovery of promising alternatives such as transition metal oxides, (oxy)hydroxides, nitrides, sulfides, and phosphides, the development of rationally designed, high-efficiency catalysts remain a formidable challenge [5–7].

Metal-organic frameworks (MOFs), a class of porous coordination polymers renowned for their unique structure, high specific surface area, and well-defined metal centers, have garnered significant interest in OER-based electrochemistry [8,9]. Among diverse MOFs-based electrocatalysts, Ni-based variants exhibit considerable research potential due to the abundance and cost-effectiveness of Ni compared to precious metal benchmarks, coupled with the advantageous redox properties of Ni's active site [10–12]. Nevertheless, numerous efforts have been given to achieving the optimal catalytic performance. Firstly, the development of multi-metal MOFs stands out as a prevalent approach to enhance catalytic performance, with some studies highlighting the significant nickel-iron synergistic impact on Ni-based MOF catalysis [8,13]. For example, Zhu et al. demonstrated that the Fe-O-Ni-O-Fe bonding in Fe-doped-(Ni-MOFs)/FeOOH facilitates OER ability (210 mV@15 mA cm^{-2}) [14]. Guan et al. proposed a NiFe MOF with low overpotentials of 189 mV at 10 mA cm^{-2} and 260 mV at 500 mA cm^{-2} for OER [15]. Secondly, coupling MOFs with other functional materials to form heterojunctions is also a good way to optimize the internal

* Corresponding authors.
E-mail addresses: jyguo@gxnu.edu.cn (J. Guo), caidandan86@163.com (D. Cai), xlyang@gxnu.edu.cn (X. Yang).

https://doi.org/10.1016/j.apcatb.2025.125105
Received 14 November 2024; Received in revised form 3 January 2025; Accepted 26 January 2025
Available online 31 January 2025

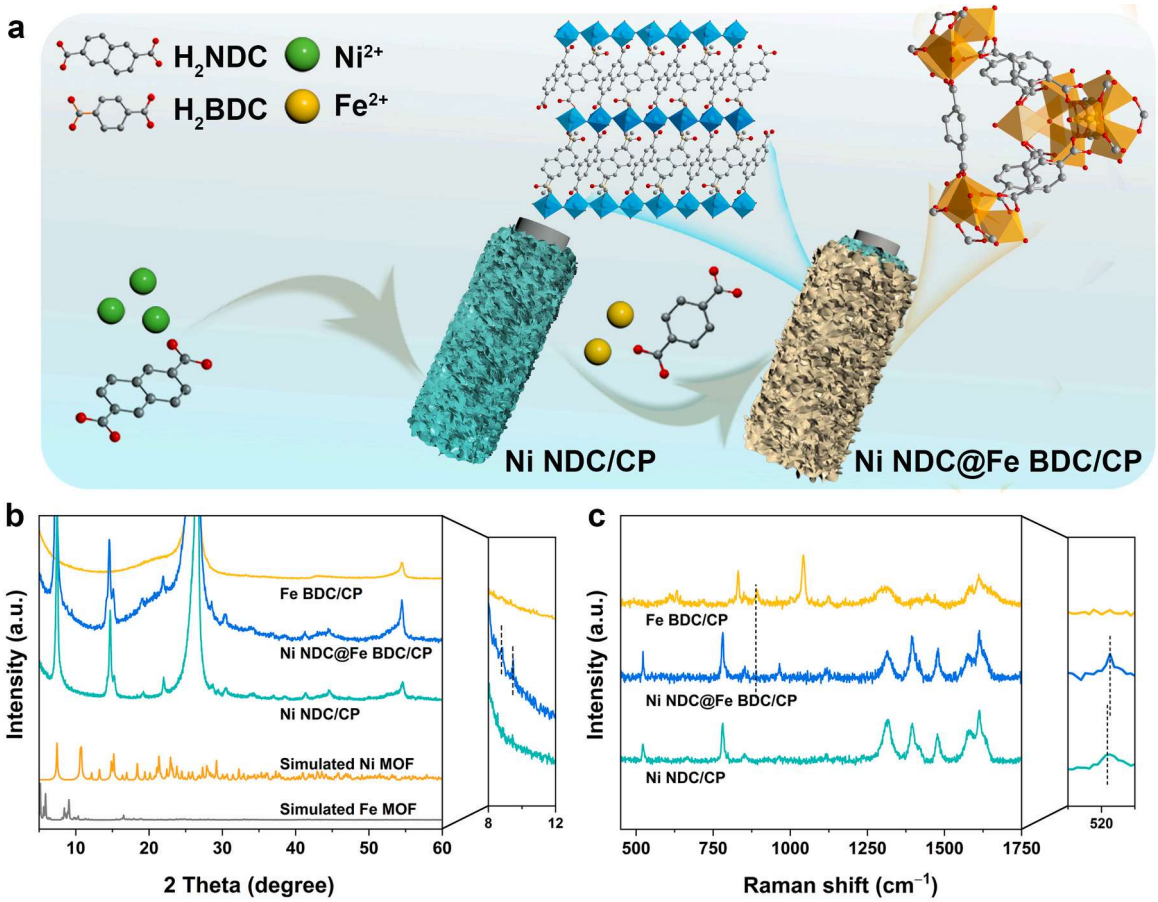

Fig. 1. (a) Schematic illustration of the synthesis of Ni NDC@Fe BDC/CP, (b) XRD patterns of simulated Ni MOF, simulated Fe MOF, Ni NDC/CP, Fe BDC/CP and Ni NDC@Fe BDC/CP, and (c) Raman spectra of Ni NDC/CP, Fe BDC/CP, Ni NDC@Fe BDC/CP and CP.

coordination of MOFs [14,16]. Notably, the assembly of composite MOF-on-MOF heterostructures has shown surprising catalytic activities in MOF-based electrocatalysis. For instance, Zhu et al. synthesized Ni-MOF@Fe-MOF, exhibiting modest electrocatalytic OER activity (265 mV@10 mA cm^{-2}) [17]. In parallel with the above tactics, introducing defects in MOFs has proven beneficial for enhancing catalytic capacity [18]. Creating oxygen vacancies through heteroatom doping has effectively modulated the surface electronic structure and optimized hydroxyl adsorption during alkaline OER, thereby improving the catalytic activity and durability of the catalysts [19–21]. Additionally, hybridizing MOFs with self-supporting substrates, such as nickel foam, iron foam, carbon cloth, and carbon paper, has been reported to accelerate the OER reaction [22,23]. Unfortunately, most MOF-on-MOF are formed by lattice matching and this synthetic strategy is limiting as most MOFs have different unit cell parameters and coordination patterns, which severely inhibits the diversity of MOF-on-MOF composites [24]. Therefore, developing feasible strategies that permit the construction of vacancy-rich MOF-on-MOF heterostructures without the limitations of lattice matching is of great significance.

Based on these considerations, the Ni NDC@Fe BDC/CP heterostructure electrocatalyst with abundant oxygen vacancies was successfully fabricated using an in situ self-optimizing assembly strategy. Ni NDC/CP precursors are initially formed through a solvothermal method, followed by the in-situ construction of Fe BDC on the Ni NDC surface to form Ni NDC@Fe BDC/CP. This in-situ growth ensures close contact and strong electronic coupling between heterogeneous interfaces. Experimental results reveal that the catalyst combines the favorable conditions of multicomponent material hybridization, ultrathin nanosheets, and defect induction, facilitating accelerated electron transfer/redistribution and an increased number of active sites, thereby effectively enhancing the intrinsic activity of catalyst. The obtained Ni NDC@Fe BDC/CP exhibits higher OER activity with a low overpotential of 192 and 239 mV at a current density of 10 and 100 mA cm^{-2}, a small Tafel slope of 38.8 mV dec^{-1}, and maintains long-term stability over 100 h at 100 mA cm^{-2}. The water splitting device assembled from Ni NDC@Fe BDC/CP and Pt/C/CP requires only 1.43 and 1.54 V to reach 10 and 100 mA cm^{-2}, respectively, maintaining a stability of over 50 h at 100 mA cm^{-2} without any performance degradation. In situ characterization confirms that Ni(Fe)OOH with abundant oxygen vacancies is the actual active species in the catalytic reaction, and density functional theory calculations further elucidate the intrinsic mechanism.

2. Experimental

2.1. Materials

The reagents were supplied by the supplier without purification. Naphthalene-2,6-dicarboxylic acid (H_2NDC, $C_{12}H_8O_4$, 98 %), terephthalic acid (H_2BDC, $C_8H_6O_4$, 98 %), nickel (II) chloride hexahydrate ($NiCl_2{\cdot}6\,H_2O$, 98 %), iron (II) chloride tetrahydrate ($FeCl_2{\cdot}4\,H_2O$, 99 %), and potassium hydroxide (KOH, 90 %) were purchased from Aladdin Chemical Reagent Co. Ltd. Absolute ethanol (EtOH, 99.7 %), absolute methanol (MeOH, 99.7 %) and N, N-dimethylformamide (DMF, 98 %) were purchased from Xilong Chemical Reagent Co. Ltd. The carbon fiber paper (CP) purchased from Toray Co. Ltd. and was utilized with a dimension of 2 cm × 1 cm in the experiments. Commercial Pt/C (20 wt% Pt) and Nafion solution (5 wt%) were purchased from Alfa Aesar. The RuO_2 was prepared by directly pyrolysis of $RuCl_3$ in air at 400 °C and

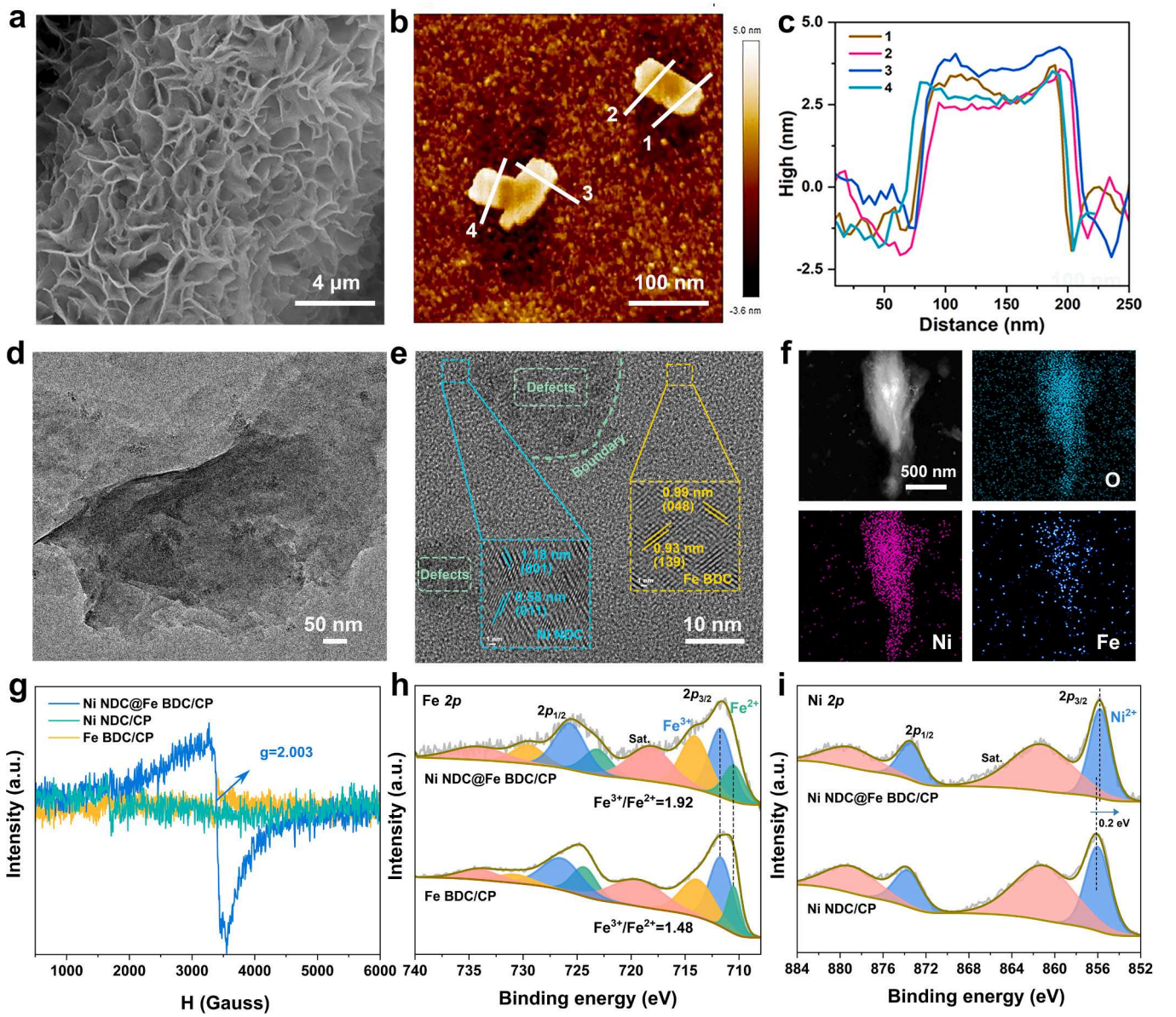

Fig. 2. (a) SEM image, (b) AFM image, (c) corresponding height profiles, (d) TEM image, (e) HR-TEM image, and (f) HAADF-STEM and corresponding EDS mapping of Ni NDC@Fe BDC/CP. (g) EPR spectra, and (h) Fe *2p* and (i) Ni *2p* XPS spectra of Ni NDC/CP, Ni NDC@Fe BDC/CP and Fe BDC/CP.

$RuCl_3{\cdot}3\ H_2O$ (37 %) were purchased from Inno-chem. The corresponding XRD pattern was indexed to RuO_2 (JCPDS: 40–1290), confirming the successful preparation of RuO_2 (Fig. S1).

2.2. Treatment of CP

The surface of CP was hydrothermally modified with 68 % HNO_3 at 120 °C for 180 min, and then cleaned with deionized water and absolute ethanol.

2.3. Synthesis of Ni NDC/CP

$NiCl_2{\cdot}6\ H_2O$ (1 mmol) and H_2NDC (0.75 mmol) were dissolved in 15 mL of mixed solution (V_{DMF}: V_{MeOH}=1:1). The resulting solution was then transferred to a 25 mL Taflon-lined stainless-steel autoclave with two pieces of modified CP. The autoclave was sealed at 120 °C and kept for 9 h in an oven. After natural cooling to room temperature, the samples were washed three times with absolute ethanol and dried 60 °C for 8 h.

2.4. Synthesis of Fe BDC/CP

The Fe BDC/CP was synthesized using a similar method as the Ni NDC/CP, with only difference being the reaction solution and reaction time. The reaction solution consisted of 16 mL of a mixed solution containing 1.25 mmol H_2BDC, 0.4 mmol $FeCl_2{\cdot}4\ H_2O$, 14 mL of DMF, 1 mL EtOH and 1 mL deionized water (DI). The reaction time was adjusted to 2 h.

2.5. Synthesis of Ni NDC@Fe BDC/CP

The synthesis of Ni NDC@Fe BDC/CP followed the same method as Fe BDC/CP, apart from the replacement of pure CP with Ni NDC/CP. Furthermore, the Ni NDC@Fe/CP and Ni NDC-BDC/CP were prepared using the exact similar method Ni NDC@Fe BDC/CP, except that the mixture of H_2BDC and $FeCl_2{\cdot}4\ H_2O$ was changed to a single $FeCl_2{\cdot}4\ H_2O$ and H_2BDC, respectively.

2.6. Synthesis of RuO_2/CP and Pt/C/CP

For comparison, RuO_2 and Pt/C on CP were also prepared. A homogeneous catalyst ink is formed by dispersing 2 mg RuO_2 or Pt/C in 250 μL deionized water/isopropyl alcohol (V / V=1:1) and 25 μL 5 % Nafion as a binder. The mixture is then dropped on the surface of the CFP (1 cm × 0.5 cm) and cools to room temperature.

3. Results and discussion

3.1. Structural and morphological characterizations

The synthesis of Ni NDC@Fe BDC/CP nanosheets involved a straightforward stepwise solvothermal process (Fig. 1a). Initially, Ni NDC nanosheets were grown on the CP backbone using $NiCl_2{\cdot}6\,H_2O$ and H_2NDC as precursors. Subsequently, the resulting Ni NDC/CP was immersed in a secondary growth solution containing $FeCl_2{\cdot}4\,H_2O$ and H_2BDC to form the Ni NDC@Fe BDC/CP. During this process, Ni NDC released Ni ions under the alkaline conditions introduced by DMF-DI-EtOH. Considering the similar radii of Ni and Fe, ion exchange occurred on the surface of Ni NDC, along with coordination between H_2BDC and metal ions. Notably, despite H_2BDC and H_2NDC being carboxylic acid ligands, the synthesized Fe BDCs and Ni NDCs exhibit markedly different topologies (Table S1). This structural distinction enables the epitaxial growth of MOF-on-MOF heterojunctions through a dynamic self-optimization process that accommodates lattice mismatches. As reported in the literature, such heterojunction interfaces can induce interfacial electron redistribution and introduce significant defects, which are critical in enhancing catalytic performance [25].

The crystal structure of Ni NDC@Fe BDC/CP was analyzed using X-ray diffraction (XRD). In Fig. 1b, all samples exhibit sharp diffraction peaks around 26.6° and 54.8°, originating from the CP substrate (JCPDS: 26–1077) [26]. For Ni NDC@Fe BDC/CP, the peaks at around 7.4°, 14.8° and 15.1° correspond to the (001), $(0\bar{1}2)$ and (011) crystal plane of Ni NDC, respectively [27]. Peaks at approximately 8.8° and 9.4° originate from the (048) and (139) crystal planes of Fe BDC [28,29]. These results confirm the synthesis of the MOF-on-MOF heterostructure. Additionally, compared with Ni NDC/CP, single Fe BDC/CP was challenging to detect due to the lower loading on CP, and more detailed local amplification of Fe BDC/CP is shown in Fig. S2. Raman spectroscopy was employed to investigate the chemical structures of Ni NDC/CP, Fe BDC/CP and Ni NDC@Fe BDC/CP (Fig. 1c). All materials displayed characteristic peaks of organic ligands in the range of 1100–1750 cm^{-1}, implying the successful preparation of MOFs. For Ni NDC@Fe BDC/CP, in addition to the original characteristic peaks of H_2NDC, a new peak at 875 cm^{-1} is attributed to the vibrations of the C-H and benzene rings in the H_2BDC, demonstrating the coexistence of the H_2NDC and H_2BDC ligands. Meanwhile, the peak of Ni-O bonding vibration in Ni NDC@Fe BDC/CP is slightly blue shifted compared to that in Ni NDC/CP (partial enlargement of Fig. 1c), which can be attributed to the phonon confinement effect induced by the surface oxygen vacancies and also reveals the reinforced Ni-O bonding in Ni NDC@Fe BDC/CP [30,31].

Scanning electron microscopy (SEM) and transmission electron microscopy (TEM) were employed to examine the morphological characteristics of Ni NDC/CP, Fe BDC/CP and Ni NDC@Fe NDC/CP. In the SEM image, the Ni NDC/CP precursor exhibits a smooth and ultra-thin nanosheet morphology (Fig. S3). With the absence of Ni NDC/CP precursors, bare Fe BDC nanoparticles are severely agglomerated on CP (Fig. S4). For Ni NDC@Fe BDC/CP, the ultra-thin nanosheet morphology is maintained, but the surface becomes slightly rougher due to the introduction of Fe BDC. This may be favorable for the mass transfer of O_2 and electrolyte during the electrocatalytic process (Figs. 2a and 2d). Atomic force microscope (AFM) measurements confirm that the Ni NDC@Fe BDC with an average thickness of about 4.3 nm (Fig. 2b-c). In the high-resolution TEM (HR-TEM) image, lattice fringe spacings of 0.99 nm and 0.93 nm correspond to the (048) and (139) crystal planes of Fe BDC, respectively. Similarly, lattice fringe spacings of 1.18 nm and 0.58 nm correspond to the (001) and (011) crystal planes of Ni NDC. These observations further confirm the successful synthesis of Ni NDC@Fe BDC (Fig. 2e) [30,32]. Notably, not all lattice breaks are continuous, and numerous dislocations and distortions are present in the Ni NDC@Fe BDC/CP (as shown by the dashed box in Fig. 2e), indicating the presence of a significant number of defects in the prepared catalyst [33,34]. Corresponding energy-dispersive X-ray spectroscopy (EDS) mapping spectra in Fig. 2f clearly show the highly uniform distribution of O, Ni, and Fe, confirming the presence of ion exchange during the secondary growth process. The more precise elemental content was determined by inductively coupled plasma mass spectrometry (ICP-MS), revealing approximately 12.1 wt% for Ni species and 3.6 wt% for Fe species (Table S2).

Electron paramagnetic resonance (EPR) spectra were determined to gain further insight into the nature of the vacancies (Fig. 2g). As reported previously, the broad peak at around 3500 Gauss in both samples can be assigned to magnetism caused by unpaired electrons, where the intensity is considered to be related to the amounts of unpaired electrons and charge localization in materials [35]. Compared to Ni NDC/CP and Fe BDC/CP, Ni NDC@Fe BDC/CP shows abundant oxygen vacancies and produces a stronger EPR signal at g= 2.003. This observation is consistent with the earlier proposal that there are more oxygen vacancies at the lattice mismatch growth interface.

X-ray photoelectron spectroscopy (XPS) was conducted to elucidate the chemical composition and elemental valence of Ni NDC/CP, Ni NDC@Fe BDC/CP and Fe BDC/CP. In Fig. S5, the full survey spectrum of Ni NDC@Fe BDC/CP demonstrates the co-existence of O, Ni and Fe, aligning perfectly with the previous EDS mapping results. The presence of Ni^{2+} oxidation state is supported by the Ni *2p* spectrum (Fig. 2i), with characteristic peaks at 856 and 873.1 eV assigned to Ni^{2+} $2p_{2/3}$ and Ni^{2+} $2p_{1/2}$, respectively [36]. In comparison to pure Ni NDC/CP, the Ni *2p* peak of Ni NDC@Fe BDC/CP is shifted to a lower binding energy, indicating a modification in the electronic local environment of Ni [37]. As for Fe *2p* spectrum (Fig. 2h), the peaks located at the binding energy of 711.8 and 725.9 eV were corresponding to Fe^{3+}, while the peaks at 710.4 and 723.4 eV were attributed to Fe^{2+}. Apparently, the ratio of Fe^{3+}/Fe^{2+} in Ni NDC@Fe BDC/CP (1.92) is larger than that in Fe BDC/CP (1.48), signifying an increased presence of Fe^{3+} species in the MOF-on-MOF heterojunction through the bridging oxygen of organic ligands, potentially contributing to enhanced electrocatalytic properties [38]. Similarly, in the O *1 s* spectra (Fig. S6), the peaks near 529.8, 531.2 and 532.5 eV have been defined as metal-oxygen bonds (M-O), oxygen vacancy defects (O_v) and absorbed water, respectively [39]. Notably, the O *1 s* peaks of single metal MOFs were fitted to C-O/C═O, M-O and H_2O_{ads} due to the absence of oxygen vacancies (Fig. S7) [8,40]. Overall, these results indicate the presence of a Ni-Fe synergistic effect and defective oxygen in Ni NDC@Fe BDC/CP, providing essential conditions for high-efficiency catalytic performance.

3.2. Electrocatalytic performance

In preliminary experiments, Ni NDC@Fe BDC/CP was prepared with different Fe BDC concentrations by adding 0.5, 1.0, and 2.0 mmol mixed solutions of Fe BDC. They were named as Ni NDC@Fe $BDC_{0.5}$, Ni NDC@Fe BDC_1, and Ni NDC@Fe BDC_2, with OER testing revealing that Ni NDC@Fe BDC_1 exhibited excellent OER activity. Subsequently, the reaction time was varied to 0.5, 2, and 6 h, resulting in Ni NDC@Fe BDC-0.5, NDC@Fe BDC-2 and Ni NDC@Fe BDC-6. The OER testing results demonstrated that Ni NDC@Fe BDC-2 displayed the best OER performance (Fig. S8). Moreover, OER activity of Ni NDC@Fe BDC/CP under acidic (0.5 M H_2SO_4) and neutral (1.0 M phosphate-buffered saline, PBS) conditions were studied. As illustrated in Fig. S9, Ni NDC@Fe BDC/CP fails to demonstrate appreciable OER performance under both 0.5 M H_2SO_4 and 1.0 M PBS. Hence, the catalytic capability of Ni NDC@Fe

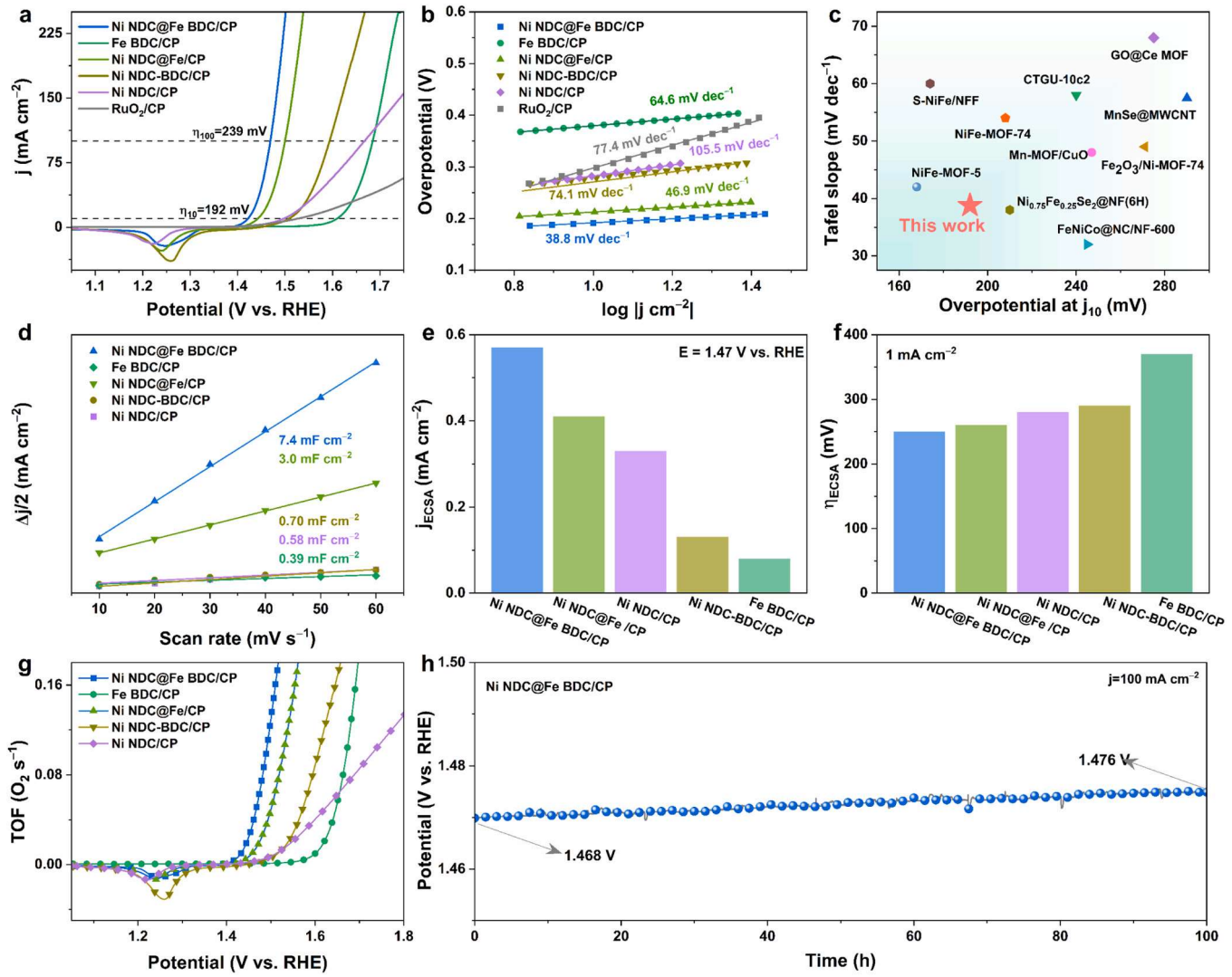

Fig. 3. (a) Linear sweep voltammetry (LSV) curves of Ni NDC@Fe BDC/CP, Ni NDC/CP, Fe BDC/CP, Ni NDC@Fe/CP, Ni NDC-BDC/CP and RuO_2/CP in OER, (b) corresponding Tafel slope derived from the LSV curves, (c) comparison the overpotential at 10 mA cm^{-2} and Tafel slope with previously reported catalysts, (d) corresponding C_{dl} values, (e) ECSA-normalized current density at an potential of 1.47 V vs. RHE, (f) Overpotentials at the current density of 1 mA cm^{-2} and (g) TOF value of as-prepared samples. (h) Chronopotentiometry curve of Ni NDC@Fe BDC/CP.

BDC/CP was investigated based on Ni NDC@Fe BDC-2 in 1.0 M KOH. For comparison, Ni NDC/CP, Fe BDC/CP, Ni NDC@Fe/CP, Ni NDC@BDC/CP, RuO_2/CP and the bare CP were also examined with corrected for 95 % *iR* using a standard three-electrode system (Fig. S10).

For accurate OER evaluation of Ni-based catalysts, we adopted reverse scanning, which eliminates oxidation peak interference, enabling reliable overpotential measurements and clearer insights into catalytic activity. As shown in Fig. 3a, the optimized Ni NDC@Fe BDC/CP exhibited overpotential of 192 mV at a current density of 10 mA cm^{-2}, which is lower than those of Ni NDC@Fe/CP (214 mV), Ni NDC@BDC/CP (280 mV), Ni NDC/CP (273 mV), RuO_2/CP (298 mV) and Fe BDC/CP (381 mV). At a current density of 100 mA cm^{-2}, the Ni NDC@Fe BDC/CP is also good with the overpotential of 239 mV, which is competitive with other samples (Table S3). Tafel slopes of all prepared catalysts were calculated to evaluate the kinetics of electrochemical OER process. Among them, Ni NDC@Fe BDC/CP exhibited lower Tafel slope value of 38.8 mV dec^{-1} than Ni NDC@Fe/CP (46.9 mV dec^{-1}), Ni NDC@BDC/CP (74.1 mV dec^{-1}), Ni NDC/CP (97.4 mV dec^{-1}), RuO_2/CP (77.4 mV dec^{-1}) and Fe BDC/CP (64.6 mV dec^{-1}), indicating fast electrocatalytic dynamics of Ni NDC@Fe BDC/CP (Fig. 3b). It is worth mentioning that Ni NDC@Fe BDC/CP is also superior to reported other OER catalysts (Fig. 3c, Table S4). The charge-transfer kinetics was further investigated by electrochemical impedance spectroscopy (EIS). The Nyquist plot of the electrode and the associated equivalent circuit model are shown in Fig. S11, where R_s is the solution resistance of the electrolyte, R_{ct} is the charge transfer resistance and CPE_{ct} is related to the electron transport of the catalyst. Compared to other samples, Ni NDC@Fe BDC/CP deliberate the lowest R_{ct}, revealing that the Ni NDC@Fe BDC/CP electrocatalyst has a high conductivity and a quick electron transfer rate [41].

In addition, the electrochemical active surface area (ECSA) value is an important standard for visualizing the surface-area activity: a larger ECSA value means more active sites. The ECSA is linearly proportional to the double layer capacitance (C_{dl}), which can be calculated by cyclic voltammetry test in non-Faraday region with different scan rates (Fig. S12). As what we expected, the Ni NDC@Fe BDC/CP shows a larger C_{dl} (7.4 mF cm^{-2}) than other samples (Fig. 3d), demonstrating the high specific surface area of the catalyst. Then, the ECSA normalized LSV curves were calculated to understand the intrinsic activity of different catalysts. As shown in Fig. S13, the ECSA normalized LSV curve indicates that the OER ability of Ni NDC@Fe BDC/CP was intrinsically improved. The ECSA-normalized current density for Ni NDC@Fe BDC/

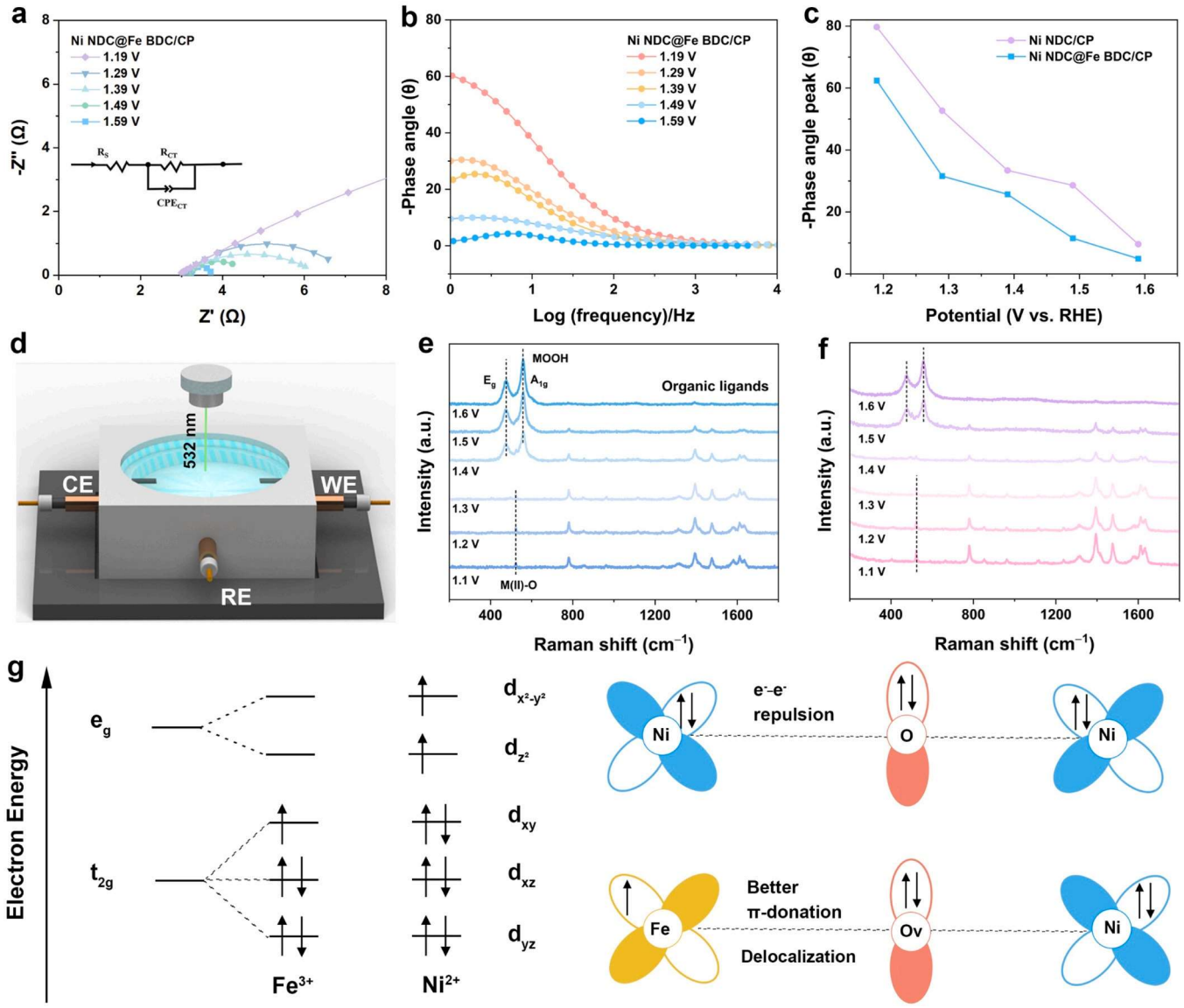

Fig. 4. (a) Nyquist plots of Ni NDC@Fe BDC/CP at different applied potentials (vs. RHE) in 1 M KOH and (b) corresponding bode plot acquired through in situ EIS measurement. (c) Phase peak angles of Ni NDC@Fe BDC/CP and Ni NDC/CP at 1.19–1.59 V vs. RHE. (d) Schematic diagram of electrochemical in-situ Raman cell. Electrochemical in situ Raman spectra of (e) Ni NDC@Fe BDC/CP and (f) Ni NDC/CP in the potential range of 1.1–1.6 V (vs. RHE). (g) The molecular orbital picture of Ni NDC@Fe BDC/CP.

CP was estimated to be 0.56 mA cm^{-2} at the potential of 1.47 V (vs. RHE), which was higher than other catalysts (Fig. 3e). Besides, the overpotential of Ni NDC@Fe BDC/CP at 1 mA cm^{-2} was only 250 mV, which was clearly lower than that of pristine Ni NDC/CP (290 mV) (Fig. 3f). Notably, the turnover frequency (TOF) is also an important parameter for comparing the intrinsic activity of catalysts [42]. The TOF values of Ni NDC@Fe BDC/CP were higher than those of the other compounds, which strongly highlights that the Ni NDC@Fe BDC/CP has more accessible active sites and higher intrinsic activity (Fig. 3g) [43]. Besides electrocatalytic activity, the stability of catalysts is also critical for practical applications. The long-term stability of the catalysts was verified by constant current tests in 1.0 M KOH. At a current density of 100 mA cm^{-2}, Ni NDC@Fe BDC/CP maintained excellent stability with no significant degradation over 100 h compared to Ni NDC/CP, indicating its excellent stability (Fig. 3h and Fig. S14).

In situ EIS under different voltages was applied to obtain more detailed information on the enhanced charge transfer kinetics of Ni NDC@Fe NDC/CP, and the corresponding fitted equivalent circuit model is shown in Fig. 4a. As seen from the Nyquist plots, it is obviously that Ni NDC@Fe BDC/CP shows lower charge transfer resistance over the applied potential range, implying that the strong heterostructure coupling effect facilitates interfacial charge transfer, which could also favor surface activation of the catalyst (Fig. 4a and S15a) [44,45]. According to the previous reports, R_{ct} was used to describe the adsorption resistance of oxygen-containing reactive species ions, and the change trend of R_{ct} revealed the OH* evolution occurring on the catalyst surface [46]. From the fitting results changes for the R_{ct} in Fig. S15c, the R_{ct} of Ni NDC@Fe BDC/CP is lower than that of Ni NDC/CP at any applied potential, which reflects its faster adsorption kinetics of oxygen-containing intermediates during OER process. Corresponding Bode plots of Ni NDC@Fe BDC/CP are portrayed in Fig. 4b and S15b. The phase peak for Ni NDC@Fe BDC/CP at the low frequency interface shows a lower phase angle at each applied potential, which can be attributed to the faster deprotonation of intermediates during the OER process and is consistent with the just-mentioned C_{dl} and ECSA normalized LSV results (Fig. 4c) [47].

More details on the local environment of the catalyst under operating conditions were obtained by using in situ Raman spectroscopy (Fig. 4d).

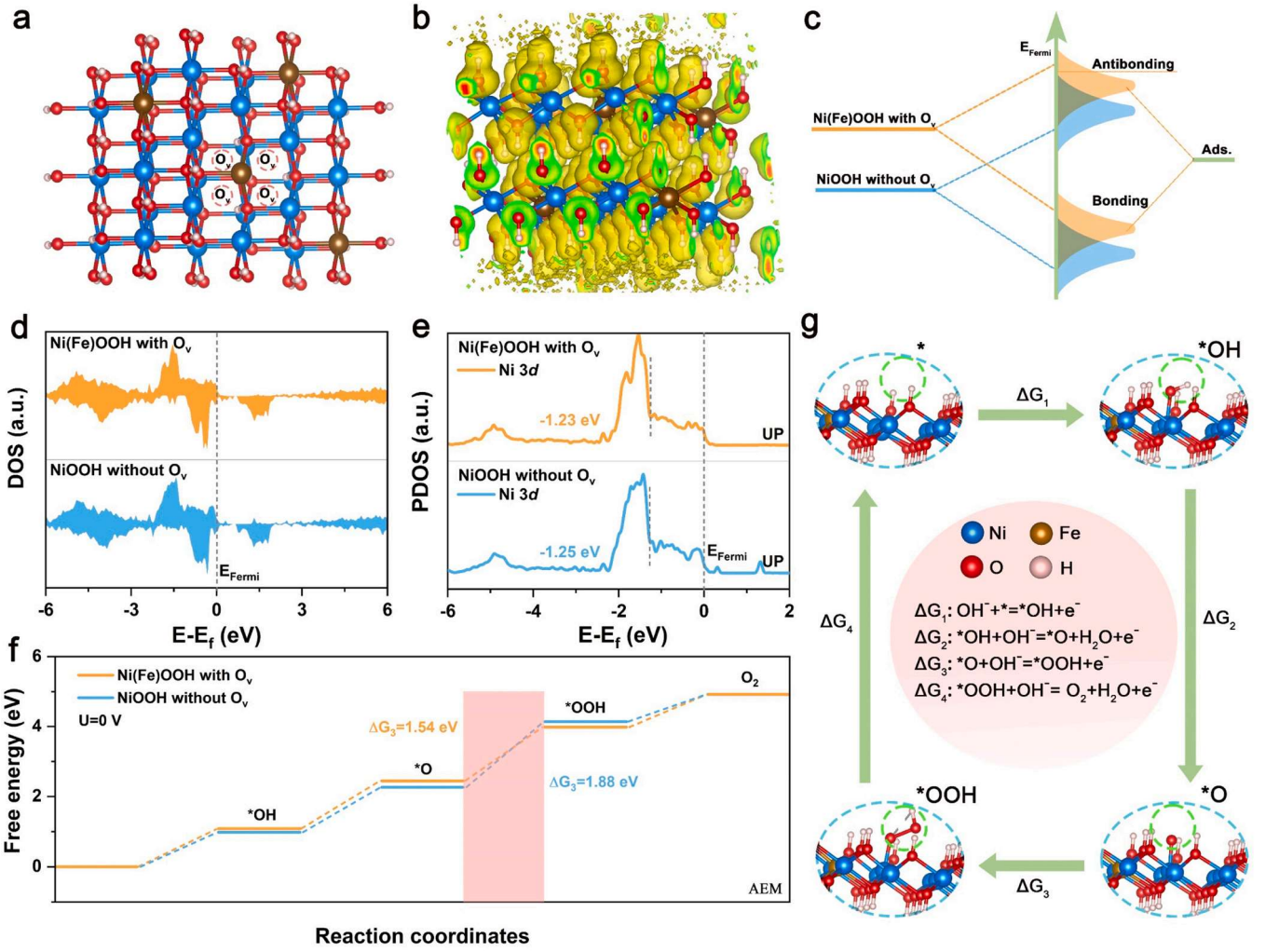

Fig. 5. (a) The local ball-and-stick model and (b) local charge density of Ni(Fe)OOH with O_v. (Blue is Ni, brown is Fe, red is O, white is H, chartreuse is an electron-rich region, and colorless is the electron-deficient region.) (c) Schematic illustration of bond formation between adsorbates (Ads.) and electrocatalysts surface. The calculated (d) DOS and (e) PDOS of Ni 3d for Ni(Fe)OOH with O_v and NiOOH without O_v. (f) OER Gibbs free energy diagrams for Ni(Fe)OOH with O_v and NiOOH without O_v. (g) Schematic of the OER catalytic mechanism for Ni(Fe)OOH with O_v.

Clearly, with the gradually increasing applied potential, original MOF disappears and is supplanted by the characteristic peaks of Ni(Fe)OOH E_g bending vibration and A_{1g} stretching vibration [48]. Compared to Ni NDC, the Ni NDC@Fe BDC heterostructure generates MOOH active phases at a lower potential. This demonstrates that constructing a defective MOF-on-MOF heterojunction not only enhances the intrinsic activity of Ni NDC but also accelerates the transformation of precatalysts into active species during electrochemical processes (Figs. 4e and 4f). Specifically, this enhanced intrinsic activity can be explained by crystal field theory (Fig. 4g). In Ni NDC, the t_{2g} orbital of Ni^{2+} is fully occupied, leading to strong electron repulsion between Ni^{2+} and bridging O^{2-} [49]. After introducing Fe BDC, the H_2BDC organic ligand with Fe^{3+} coordination is a strong field ligand, its d-orbital splitting energy is higher than the pairing electron energy, resulting in the valence electronic configuration of Fe^{3+} being $t_{2g}^5e_g^0$ with a low spin state [50]. Compared with Ni NDC, the presence of oxygen vacancies at the heterojunction interface of Ni NDC@Fe BDC not only fosters the electron delocalization at the Fe-O bonds, but also allows the ample localized electrons in Ni-O bonds to migrate to the Ni centers, thus enhancing the electronic properties and catalytic reactivity via a complex manner [51]. Additionally, when electrons are transferred from Fe to Ni, the electrons in the Fe 3d orbitals can be rearranged to produce high spin Fe species [50]. In all, this electron transfer optimizes the electron distribution on the t_{2g} orbitals and is more favorable for the adsorption of active intermediates [52].

According to the XRD, TEM、EPR and XPS analyses were conducted on the stability-tested Ni NDC@Fe BDC/CP. The XRD spectra shows the disappearance of the characteristic MOF peaks, and the newly appeared peaks can be assigned to the NiOOH (JCPDS: 06–0075), suggesting the formation of (oxy)hydroxides (Fig. S16a) [53,54]. TEM image in Fig. S16b illustrated that the catalyst maintains the lamellar morphology after high current stabilization and HR-TEM image showed the lattice fringes of NiOOH, which is consistent with the XRD results (Fig. S16c). The corresponding EDX spectra shows a well distributed C, O, Ni and Fe elements after the OER stability test (Fig. S16d). The HR-TEM images and EPR spectra confirm that Ni NDC@Fe BDC/CP retains oxygen vacancies after the stability test (Fig. S17). As a control, EPR spectra of Ni NDC/CP post-stability testing were also analyzed, revealing that the reacted Ni NDC/CP lacks vacancies and exhibits poor catalytic activity.

Ni 2*p* XPS spectra after the stability test show new peaks at binding energies of 858.6 and 873.7 eV, corresponding to Ni^{3+}, indicating partial conversion of Ni^{2+} to high-valence Ni^{3+}, which forms more active sites (Figs. S18a and S19) [55,56]. Moreover, a significant increase in the amount of Ni^{3+} is observed in the post-OER state of Ni NDC@Fe BDC/CP compared to Ni NDC/CP. This further suggests that incorporating Fe BDC promotes the formation of a greater amount of

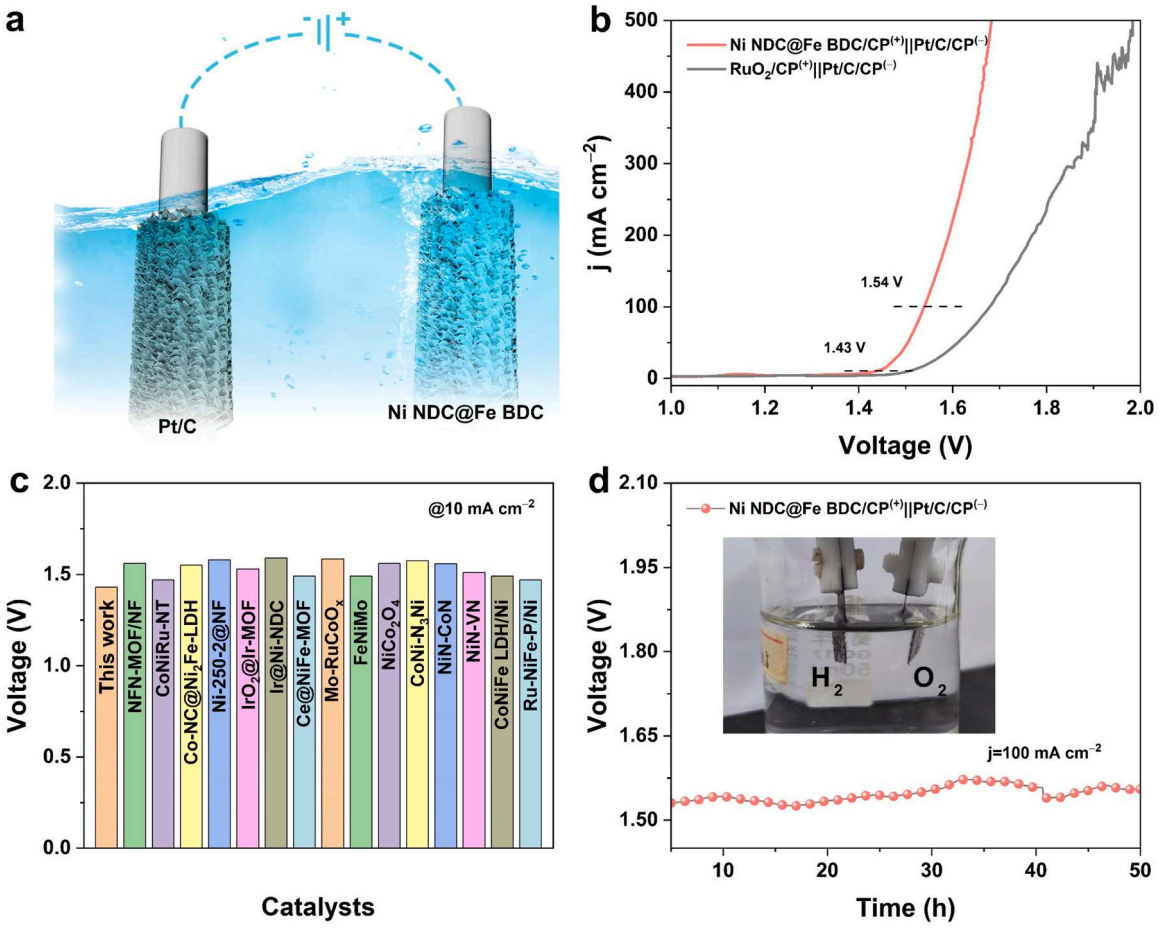

Fig. 6. (a) Schematic diagram of overall water splitting electrolyzer. (b) Comparison of the polarization curves of Ni NDC@Fe BDC/CP$^{(+)}$||Pt/C/CP$^{(-)}$ and the RuO_2/CP$^{(+)}$||Pt/C/CP$^{(-)}$ at high current densities in 1.0 M KOH. (c) Comparing cell voltages with the recently reported electrolyzers at 10 mA cm^{-2} in 1.0 M KOH. (d) Digital photo and the corresponding long-term stability test of Ni NDC@Fe BDC/CP$^{(+)}$||Pt/C/CP$^{(-)}$ at 100 mA cm^{-2} in 1.0 M KOH.

high-valence Ni species. In the Fe 2*p* XPS spectra, the Fe^{3+}/Fe^{2+} peak ratio for Ni NDC@Fe BDC/CP increases to 2.45 after the stability test, suggesting the generation of more Fe^{3+} species (Fig. S18b) [57]. From a valence electron perspective, the orbitals of Ni^{2+} and Fe^{2+} overlap and hybridize with the p-orbitals of bridging oxygen atoms in Ni(Fe)OOH, forming the distinctive Ni–O–Fe bond. Within this microenvironment, the relatively low electronegativity of Ni^{2+} and Fe^{2+}, compared to the strong electronegativity of oxygen atoms, causes the electron cloud to naturally shift from Ni^{2+} and Fe^{2+} toward the oxygen atoms, facilitating electron transfer from Ni^{2+} and Fe^{2+} to the oxygen atoms [58,59]. More detailed, the relative ratio of O_v/M-O can be used to evaluate the relative amount of oxygen vacancies; higher ratios indicate more oxygen vacancies available at the surface. In the O *1 s* XPS spectra, the relative ratio of O_v/M-O has decreased from 5.68 to 1.45 (Fig. S18c, Table S5), whereas can be explained by O_v in the Ni(Fe)OOH being easily filled with OH^- to generate active OOH* intermediate species during OER process [60]. Based on the above analysis, it can be concluded that oxygen defects play a critical role in OER by enhancing reactant activation and maintaining stability. Moderate defects prevent structural destabilization, while EPR and XPS tests confirm that although oxygen vacancies decrease in the catalyst during the OER process, they remain present. The synergy of Fe doping and oxygen vacancies underpins catalyst's superior performance.

3.3. Catalytic mechanism analysis

To elucidate the interplay between electronic structure and intrinsic catalytic mechanism, theoretical investigations based on density functional theory (DFT) calculations were conducted. Previous experimental investigations have demonstrated that Ni NDC@Fe BDC functions as a precatalyst, with the in-situ generated Ni(Fe)OOH acting as the active site for OER. Accordingly, two models were constructed for analysis: Ni(Fe)OOH with oxygen vacancies (O_v) and a pure NiOOH phase without O_v (Fig. 5a and Fig. S20). The charge density presents that there are strong electronic interactions between Ni, Fe and O, and the charge accumulation around the O atoms in Ni(Fe)OOH with O_v proving that electrons are transferred from Ni/Fe to O atoms and is in line with the XPS results (Fig. 5b). The calculated density of states (DOS) in Fig. 5d shows that Ni(Fe)OOH with O_v displays a heightened DOS near the Fermi level, indicating that more charge carriers are directly participating in the catalytic reaction, thus significantly improving the OER performance of the catalyst [61]. Meanwhile, compare to NiOOH without O_v (-1.25 eV), the d-band center (ε_d) of Ni(Fe)OOH with O_v (-1.23 eV) is closer to the Fermi level, which was beneficial for exposing active sites and adsorbing active intermediates (Fig. 5e). According to the d-band center theory, the electronic interaction between adsorbates and electrocatalysts can be interpreted as the coupling between the valence states of adsorbate and the d-band center of the transition metal, resulting in the formation of split bonding and antibonding states (Fig. 5c) [62]. The bonding states lower than the Fermi level are usually filled, whereas the antibonding state of NiOOH rises after introducing Fe doping and oxygen vacancies, leading to a higher adsorption capacity for reaction intermediates in the OER process. Subsequently, based on the widely accepted AEM mechanism under alkaline OER process and the prior experimental results, the optimal models of *OH, *O and *OOH intermediates of Ni(Fe)OOH with O_v are shown in Fig. 5g, in which Ni

site was considered as adsorption site [63]. Firstly, OH^- is absorbed at the Ni sites to form the Ni-OH group (ΔG_1). This is followed by the first deprotonation of the Ni-OH group to form the Ni-O group (ΔG_2). Then the Ni-O group combines with OH^- to form the superoxide species Ni-OOH (ΔG_3). At last, the Ni-OOH reacts with the OH^- and underwent deprotonation to produce O_2 and H_2O (ΔG_4). As shown in Fig. 5f, the conversion of *O to *OOH is the rate-determining step (RDS) for Ni(Fe)OOH with O_v and NiOOH without O_v. And the ΔG_3 of Ni(Fe)OOH with O_v (1.54 eV) was lower than that of NiOOH without O_v (1.88 eV), suggesting that the former has better OER dynamics.

3.4. Overall water splitting

Considering the remarkable OER performance of Ni NDC@Fe BDC, a two-electrode device using Ni NDC@Fe BDC/CP as the anode and Pt/C/CP as the cathode was constructed to evaluate the catalytic performance in overall water splitting (OWS) (Fig. 6a). As illustrated in Fig. 6b, Ni NDC@Fe BDC/$CP^{(+)}$||Pt/C/$CP^{(-)}$ needs cell voltage of 1.43 as well as 1.54 V at 10 and 100 mA cm^{-2}, individually, slightly lower than the of commercial RuO_2/$CP^{(+)}$||Pt/C/$CP^{(-)}$ and other previously published catalysts (Fig. 6c, Table S6). At high current densities, the polarization curves exhibit slight instability, which may be attributed to the formation and accumulation of gas bubbles on the electrode surface. As the current density increases, the electrochemical reaction rate on the electrode surface accelerates, resulting in increased hydrogen generation and rapid bubble formation. The operation of the electrolyzer is depicted in the inset digital photographs in Fig. 6d. The chronopotentiometry curve of Ni NDC@Fe BDC/$CP^{(+)}$||Pt/C/$CP^{(-)}$ at 100 mA cm^{-2} was maintain for more than 50 h, thus confirming its high durability for OWS. These results reinforce the potential of Ni NDC@Fe BDC/CP for sustainable energy applications.

4. Conclusions

In summary, we successfully engineered a vacancy-rich Ni NDC@Fe BDC/CP self-supporting electrode using an in situ self-optimization approach. It exhibits low overpotentials of 192 mV at 10 mA cm^{-2} and 239 mV at 100 mA cm^{-2}, outperforming Ni NDC/CP, Fe BDC/CP, and commercial RuO_2/CP. The Tafel slope of 38.8 mV dec^{-1} and the lowest charge transfer resistance among tested samples highlight its superior kinetics and conductivity. DFT calculations reveal a heightened density of states near the Fermi level and a favorable d-band center, facilitating active intermediate adsorption. The two-electrode device using Ni NDC@Fe BDC/CP and Pt/C/CP achieved current densities of 10 and 100 mA cm^{-2} at 1.43 and 1.54 V, respectively, with stability over 50 h at 100 mA cm^{-2}. In a word, Ni NDC@Fe BDC/CP demonstrates exceptional OER performance and stability driven by its unique structure and electronic properties, making it a promising candidate for efficient hydrogen production and sustainable energy applications. This study elucidates the potential mechanism of lattice mismatch in the epitaxial growth of MOF-on-MOF structures and presents a novel approach for designing high-performance MOF-based materials for electrocatalysis.

Declaration of Competing Interest

The authors declare that they have no known competing financial interests or personal relationships that could have appeared to influence the work reported in this paper.

Acknowledgements

This work has been supported by the National Natural Science Foundation of China (no. 22068008, 52363028, 21965005), Natural Science Foundation of Guangxi Province (2021GXNSFAA076001, 2018GXNSFAA294077), Guangxi Technology Base and Talent Subject (GUIKE AD23023004, GUIKE AD20297039).

Appendix A. Supporting information

Supplementary data associated with this article can be found in the online version at doi:10.1016/j.apcatb.2025.125105.

Data availability

Data will be made available on request.

References

[1] H.B. Wu, B.Y. Xia, L. Yu, X.Y. Yu, X.W. Lou, Porous molybdenum carbide nano-octahedrons synthesized via confined carburization in metal-organic frameworks for efficient hydrogen production, Nat. Commun. 6 (2015) 6512.
[2] L. Yan, L. Cao, P. Dai, X. Gu, D. Liu, L. Li, Y. Wang, X. Zhao, Metal-organic frameworks derived nanotube of nickel–cobalt bimetal phosphides as highly efficient electrocatalysts for overall water splitting, Adv. Funct. Mater. 27 (2017) 1703455.
[3] J. Wang, H. Kong, J. Zhang, Y. Hao, Z. Shao, F. Ciucci, Carbon-based electrocatalysts for sustainable energy applications, Prog. Mater. Sci. 116 (2021) 100717.
[4] T. Wang, X. Cao, L. Jiao, MOFs-derived carbon-based metal catalysts for energy-related electrocatalysis, Small 17 (2021) e2004398.
[5] F. Zeng, C. Mebrahtu, L. Liao, A.K. Beine, R. Palkovits, Stability and deactivation of OER electrocatalysts: a review, J. Energy Chem. 69 (2022) 301–329.
[6] A. Karmakar, K. Karthick, S.S. Sankar, S. Kumaravel, R. Madhu, S. Kundu, A vast exploration of improvising synthetic strategies for enhancing the OER kinetics of LDH structures: a review, J. Mater. Chem. A 9 (2021) 1314–1352.
[7] A. Shahzad, F. Zulfiqar, M. Arif Nadeem, Cobalt containing bimetallic ZIFs and their derivatives as OER electrocatalysts: a critical review, Coord. Chem. Rev. 477 (2023) 214925.
[8] Y. Zhu, L. Zhang, B. Zhao, H. Chen, X. Liu, R. Zhao, X. Wang, J. Liu, Y. Chen, M. Liu, Improving the activity for oxygen evolution reaction by tailoring oxygen defects in double perovskite oxides, Adv. Funct. Mater. 29 (2019) 1901783.
[9] T. Kang, J. Kim, Optimal cobalt-based catalyst containing high-ratio of oxygen vacancy synthesized from metal-organic-framework (MOF) for oxygen evolution reaction (OER) enhancement, Appl. Surf. Sci. 560 (2021) 150035.
[10] A. Goswami, D. Ghosh, V.V. Chernyshev, A. Dey, D. Pradhan, K. Biradha, 2D MOFs with Ni(II), Cu(II), and Co(II) as efficient oxygen evolution electrocatalysts: rationalization of catalytic performance vs structure of the MOFs and potential of the redox couples, ACS Appl. Mater. Interfaces 12 (2020) 33679–33689.
[11] Z. Chen, Q. Fan, J. Zhou, X. Wang, M. Huang, H. Jiang, H. Colfen, Toward understanding the formation mechanism and OER catalytic mechanism of hydroxides by in situ and operando techniques, Angew. Chem. Int. Ed. 62 (2023) e202309293.
[12] W. Zhai, Y. Chen, Y. Liu, T. Sakthivel, Y. Ma, Y. Qin, Y. Qu, Z. Dai, Enlarging the Ni-O bond polarizability in a phosphorene-hosted metal-organic framework for boosted water oxidation electrocatalysis, ACS Nano 17 (2023) 17254–17264.
[13] R. Hou, X. Yang, L. Su, W. Cen, L. Ye, D. Sun, Accelerating structure reconstruction to form NiOOH in metal-organic frameworks (MOFs) for boosting oxygen evolution reaction, Nanoscale 15 (2023) 18858–18863.
[14] C.F. Li, L.J. Xie, J.W. Zhao, L.F. Gu, H.B. Tang, L. Zheng, G.R. Li, Interfacial Fe-O-Ni-O-Fe bonding regulates the active Ni sites of Ni-MOFs via iron doping and decorating with FeOOH for super-efficient oxygen evolution, Angew. Chem. Int. Ed. 61 (2022) e202116934.
[15] S. Liu, Y. Chang, N. He, S. Zhu, L. Wang, X. Liu, Competition between lattice oxygen and adsorbate evolving mechanisms in rutile ru-based oxide for the oxygen evolution reaction, ACS Appl. Mater. Interfaces 15 (2023) 20563–20570.
[16] Y. Luo, X. Yang, L. He, Y. Zheng, J. Pang, L. Wang, R. Jiang, J. Hou, X. Guo, L. Chen, Structural and electronic modulation of iron-based bimetallic metal-organic framework bifunctional electrocatalysts for efficient overall water splitting in alkaline and seawater environment, ACS Appl. Mater. Interfaces 14 (2022) 46374–46385.
[17] K. Rui, G. Zhao, Y. Chen, Y. Lin, Q. Zhou, J. Chen, J. Zhu, W. Sun, W. Huang, S. X. Dou, Hybrid 2D dual-metal–organic frameworks for enhanced water oxidation catalysis, Adv. Funct. Mater. 28 (2018) 1801554.
[18] M. Xiao, C. Wu, J. Zhu, C. Zhang, Y. Li, J. Lyu, W. Zeng, H. Li, L. Chen, S. Mu, In situ generated layered NiFe-LDH/MOF heterostructure nanosheet arrays with abundant defects for efficient alkaline and seawater oxidation, Nano Res. 16 (2023) 8945–8952.
[19] H. Zhong, G. Gao, X. Wang, H. Wu, S. Shen, W. Zuo, G. Cai, G. Wei, Y. Shi, D. Fu, C. Jiang, L.W. Wang, F. Ren, Ion irradiation inducing oxygen vacancy-rich NiO/$NiFe_2O_4$ heterostructure for enhanced electrocatalytic water splitting, Small 17 (2021) e2103501.
[20] B. Liu, Y. Wang, H.Q. Peng, R. Yang, Z. Jiang, X. Zhou, C.S. Lee, H. Zhao, W. Zhang, Iron vacancies induced bifunctionality in ultrathin feroxyhyte nanosheets for overall water splitting, Adv. Mater. (2018) e1803144.
[21] L. Gao, C. Tang, J. Liu, L. He, H. Wang, Z. Ke, W. Li, C. Jiang, D. He, L. Cheng, X. Xiao, Oxygen vacancy-induced electron density tuning of Fe_3O_4 for enhanced oxygen evolution catalysis, Energy Environ. Mater. 4 (2020) 392–398.

[22] J. Xing, K. Guo, Z. Zou, M. Cai, J. Du, C. Xu, In situ growth of well-ordered NiFe-MOF-74 on Ni foam by Fe^{2+} induction as an efficient and stable electrocatalyst for water oxidation, Chem. Commun. 54 (2018) 7046–7049.
[23] C. Pan, Z. Liu, M. Huang, 2D iron-doped nickel MOF nanosheets grown on nickel foam for highly efficient oxygen evolution reaction, Appl. Surf. Sci. 529 (2020) 147201.
[24] W. Qin, L. He, Y. Zhang, B. Li, L. Han, Y. Xu, Synchronous wrapping and inward-etching strategy on constructing yolk-shell MIL-88A@NiFe-PB heterostructures for electrochemical non-enzymatic glucose detection, Microchem. J. 196 (2024) 109641.
[25] L.-M. Chang, Z.-Z. Ma, J. Huang, Z.-G. Gu, Liquid-phase epitaxial growth of multiple MOF thin films with high lattice mismatch, Inorg. Chem. Front. 10 (2023) 1136–1142.
[26] Y. Guo, K. Jia, F. Dai, Y. Liu, C. Zhang, J. Su, K. Wang, Hierarchical porous tri-metallic NiCoFe-Se/CFP derived from Ni-Co-Fe prussian blue analogues as efficient electrocatalyst for oxygen evolution reaction, J. Colloid Interface Sci. 642 (2023) 638–647.
[27] W. Cheng, X. Zhao, H. Su, F. Tang, W. Che, H. Zhang, Q. Liu, Lattice-strained metal–organic-framework arrays for bifunctional oxygen electrocatalysis, Nat. Energy 4 (2019) 115–122.
[28] Y. Guo, C. Feng, S. Qiao, S. Wang, T. Chen, L. Zhang, Y. Zhao, J. Wang, Magnetic Fe_3O_4-encapsulated VAN@MIL-101(Fe) with mixed-valence sites and mesoporous structures as efficient bifunctional water splitting photocatalysts, Nanoscale 12 (2020) 12551–12560.
[29] C. Bao, H. Wang, C. Wang, X. Zhang, X. Zhao, C.-L. Dong, Y.-C. Huang, S. Chen, P. Guo, X. She, Y. Sun, D. Yang, Cooperation of oxygen vacancy and Fe^{III}/Fe^{II} sites in H_2-reduced Fe-MIL-101 for enhanced Fenton-like degradation of organic pollutants, J. Hazard. Mater. 441 (2023) 129922.
[30] J. Huang, K. Li, L. Wang, H. She, Q. Wang, In situ conversion builds MIL-101@NiFe-LDH heterojunction structures to enhance the oxygen evolution reaction, Chin. Chem. Lett. 33 (2022) 3787–3791.
[31] K. Min, M. Hwang, S.E. Shim, D. Lim, S.-H. Baeck, Defect-rich Fe-doped Co_3O_4 derived from bimetallic-organic framework as an enhanced electrocatalyst for oxygen evolution reaction, Chem. Eng. J. 424 (2021) 130400.
[32] J. Yang, Y. Shen, Y. Sun, J. Xian, Y. Long, G. Li, Ir nanoparticles anchored on metal-organic frameworks for efficient overall water splitting under pH-universal conditions, Angew. Chem. Int. Ed. 62 (2023) e202302220.
[33] L. He, N. Wang, M. Xiang, L. Zhong, S. Komarneni, W. Hu, S-vacancy-rich NiFe-S nanosheets based on a fully electrochemical strategy for large-scale and quasi-industrial OER catalysts, Appl. Catal. B Environ. Energy 345 (2024) 123686.
[34] H. Huang, H. Kim, A. Lee, S. Kim, W.-G. Lim, C.-Y. Park, S. Kim, S.-K. Kim, J. Lee, Structure engineering defective and mass transfer-enhanced RuO_2 nanosheets for proton exchange membrane water electrolyzer, Nano Energy 88 (2021) 106276.
[35] J. Lee, K. Min, Y. Son, D. Ko, S.E. Shim, S.-H. Baeck, Synergistic effect of heterointerface engineering and oxygen vacancy in CoFe-layered double hydroxide/Co_3O_4 composite for boosting alkaline water oxidation, Mater. Today Chem. 33 (2023) 101716.
[36] X. Liu, S. Su, H. Yin, S. Zhang, T.T. Isimjan, J. Huang, X. Yang, D. Cai, Precise anchoring of Fe sites by regulating crystallinity of novel binuclear Ni-MOF for revealing mechanism of electrocatalytic oxygen evolution, Small (2023) e2306085.
[37] J.B. Pan, B.H. Wang, J.B. Wang, H.Z. Ding, W. Zhou, X. Liu, J.R. Zhang, S. Shen, J. K. Guo, L. Chen, C.T. Au, L.L. Jiang, S.F. Yin, Activity and stability boosting of an oxygen-vacancy-rich $BiVO_4$ photoanode by NiFe-MOFs thin layer for water oxidation, Angew. Chem. Int. Ed. 60 (2021) 1433–1440.
[38] S. Peng, R. Li, Y. Rao, Y. Huang, Y. Zhao, M. Xiong, J. Cao, S. Lee, Tuning the unsaturated iron sites in MIL-101(Fe) nanoparticles for reactive oxygen species-mediated bacterial inactivation in the dark, Appl. Catal. B Environ. Energy 316 (2022) 121693.
[39] L. Que, L. Lu, Y. Xu, X. Xu, M. Zhu, J. Pan, J. Cao, J. Wang, Y. Zheng, C. Li, The Ni^{2+}-$LaNiO_3$/CdS hollow core–shell heterojunction towards enhanced visible light overall water splitting H_2 evolution via HER/OER synergism of Ni^{2+}/O_v, Chem. Eng. J. 469 (2023) 143902.
[40] R. Zhang, L. Pan, B. Guo, Z.F. Huang, Z. Chen, L. Wang, X. Zhang, Z. Guo, W. Xu, K. P. Loh, J.J. Zou, Tracking the role of defect types in Co_3O_4 structural evolution and active motifs during oxygen evolution reaction, J. Am. Chem. Soc. 145 (2023) 2271–2281.
[41] R. Guo, H. Wen, S. Zhang, T. Yu, Y. He, Z. Ni, J. You, Anionic sulfur-modified FeNi-LDH at various Fe/Ni molar ratios for high-performance OER electrocatalysis, Mater. Lett. 285 (2021) 129132.
[42] Z. Abdi, M. Vandichel, A.S. Sologubenko, M.-G. Willinger, J.-R. Shen, S. I. Allakhverdiev, M.M. Najafpour, The importance of identifying the true catalyst when using Randles-Sevcik equation to calculate turnover frequency, Int. J. Hydrog. Energy 46 (2021) 37774–37781.
[43] Y. Shi, S. Zhou, J. Liu, X. Zhang, J. Yin, T. Zhan, Y. Yang, G. Li, J. Lai, L. Wang, An integrated amorphous cobalt phosphoselenide electrocatalyst with high mass activity boosts alkaline overall water splitting, Appl. Catal. B Environ. Energy 341 (2024) 123326.
[44] X. Chen, Q. Wang, Y. Cheng, H. Xing, J. Li, X. Zhu, L. Ma, Y. Li, D. Liu, S-doping triggers redox reactivities of both iron and lattice oxygen in FeOOH for low-cost and high-performance water oxidation, Adv. Funct. Mater. 32 (2022) 2112674.
[45] Q.N. Bian, B.S. Guo, D.X. Tan, D. Zhang, W.Q. Kong, C.B. Wang, Y.Y. Feng, Constructing CoNi-LDH/Fe MOF/NF heterostructure catalyst for energy-efficient OER and UOR at high current density, ACS Appl. Mater. Interfaces 16 (2024) 14742–14749.
[46] Z. Xiao, Y.C. Huang, C.L. Dong, C. Xie, Z. Liu, S. Du, W. Chen, D. Yan, L. Tao, Z. Shu, G. Zhang, H. Duan, Y. Wang, Y. Zou, R. Chen, S. Wang, Operando identification of the dynamic behavior of oxygen vacancy-rich Co_3O_4 for oxygen evolution reaction, J. Am. Chem. Soc. 142 (2020) 12087–12095.
[47] Z. Xu, W. Zuo, Y. Yu, J. Liu, G. Cheng, P. Zhao, Surface reconstruction facilitated by fluorine migration and bimetallic center in NiCo bimetallic fluoride toward oxygen evolution reaction, Adv. Sci. 11 (2024) e2306758.
[48] M. Ying, R. Tang, W. Yang, W. Liang, G. Yang, H. Pan, X. Liao, J. Huang, Tailoring electronegativity of bimetallic Ni/Fe metal–organic framework nanosheets for electrocatalytic water oxidation, ACS Appl. Nano Mater. 4 (2021) 1967–1975.
[49] H. Jungi, A. Karmakar, S. Kundu, J. Mitra, Waste is the best: end-of-life lithium ion battery-derived ultra-active Ni^{3+}-enriched β-$Ni(OH)_2$ for the electrocatalytic oxygen evolution reaction, J. Mater. Chem. A 11 (2023) 13687–13696.
[50] Z. Qian, K. Wang, K. Shi, Z. Fu, Z. Mai, X. Wang, Z. Tang, Y. Tian, Interfacial electron transfer of heterostructured MIL-88A/$Ni(OH)_2$ enhances the oxygen evolution reaction in alkaline solutions, J. Mater. Chem. A 8 (2020) 3311–3321.
[51] Z. Li, C. Zhang, Y. Yang, S. Pi, Y. Yu, C. Wan, B. Zhou, W. Chao, L. Lu, Molten-salt-induced phosphorus vacancy defect engineering of heterostructured cobalt phosphides for efficient overall water splitting, Inorg. Chem. Front. 10 (2023) 325–334.
[52] J. Zhang, M. Li, Z. Qiao, K. Huo, Y. Yang, D. Ji, D. Yuan, L. Lin, Z. Li, H. Wu, Oxygen-vacancy-mediated electron localization at the nickel sites in nickel/iron layered double hydroxide towards efficient oxygen evolution reaction, J. Mater. Chem. A 12 (2024) 2044–2052.
[53] L. Liu, Z. Zhou, C. Peng, Sonochemical intercalation synthesis of nano γ-nickel oxyhydroxide: structure and electrochemical properties, Electrochim. Acta 54 (2008) 434–441.
[54] Y. Zhang, J. Zhao, G. Fan, L. Yang, F. Li, Robust MOF-derived carbon-supported bimetallic Ni-Co catalysts for aqueous phase hydrodeoxygenation of vanillin, Dalton Trans. 51 (2022) 2238–2249.
[55] Z. Huang, S. Zhu, Y. Duan, C. Pi, X. Zhang, A. Reda Woldu, J.-X. Jian, P.K. Chu, Q.-X. Tong, L. Hu, X. Yao, Insights into ionic association boosting water oxidation activity and dynamic stability, J. Energy Chem. 89 (2023) 99–109.
[56] X.-Y. Wang, M. Zhu, Q.-N. Bian, B.-S. Guo, W.-Q. Kong, C.-B. Wang, Y.-Y. Feng, Fe-based metal–organic framework-Ni3S2 heterostructure nanocomposites for efficient oxygen evolution reaction at high current densities, ACS Appl. Nano Mater. 6 (2023) 5200–5210.
[57] C. Li, W. Zhang, Y. Cao, J.Y. Ji, Z.C. Li, X. Han, H. Gu, P. Braunstein, J.P. Lang, Interfacial electronic interactions between ultrathin NiFe-MOF nanosheets and Ir nanoparticles heterojunctions leading to efficient overall water splitting, Adv. Sci. 11 (2024) e2401780.
[58] L. Wu, M. Ning, X. Xing, Y. Wang, F. Zhang, G. Gao, S. Song, D. Wang, C. Yuan, L. Yu, J. Bao, S. Chen, Z. Ren, Boosting oxygen evolution reaction of (Fe,Ni)OOH via defect engineering for anion exchange membrane water electrolysis under industrial conditions, Adv. Mater. 35 (2023) e2306097.
[59] C. Qiao, Z. Usman, T. Cao, S. Rafai, Z. Wang, Y. Zhu, C. Cao, J. Zhang, High-valence Ni and Fe sites on sulfated NiFe-LDH nanosheets to enhance O-O coupling for water oxidation, Chem. Eng. J. 426 (2021) 130873.
[60] Z. Xiao, Y.-C. Huang, C.-L. Dong, C. Xie, Z. Liu, S. Du, W. Chen, D. Yan, L. Tao, Z. Shu, G. Zhang, H. Duan, Y. Wang, Y. Zou, R. Chen, S. Wang, Operando identification of the dynamic behavior of oxygen vacancy-rich Co_3O_4 for oxygen evolution reaction, J. Am. Chem. Soc. 142 (2020) 12087–12095.
[61] Y. Fan, J. Zhang, J. Han, M. Zhang, W. Bao, H. Su, N. Wang, P. Zhang, Z. Luo, In situ self-reconstructed hierarchical bimetallic oxyhydroxide nanosheets of metallic sulfides for high-efficiency electrochemical water splitting, Mater. Horiz. 11 (2024) 1797–1807.
[62] P. Zhao, C. Peng, Y. Luo, L. Cheng, Z. Li, Z. Jiao, Modulating positive charge sites generations and iron oxidation state transitions in FeP_4/CoP/C_{p-n} heterojunction toward efficient oxygen evolution, Appl. Catal. B Environ. Energy 483 (2024) 149121.
[63] S. Zhang, Z. Huang, T.T. Isimjan, D. Cai, X. Yang, Accurately substituting Fe for Ni_2 atom in Ni-MOF with defect-rich for efficient oxygen evolution reaction: electronic reconfiguration and mechanistic study, Appl. Catal. B Environ. Energy 343 (2024) 123448.